A toughening design for stretchable composite embedded with strain-rate stiffening elastomer

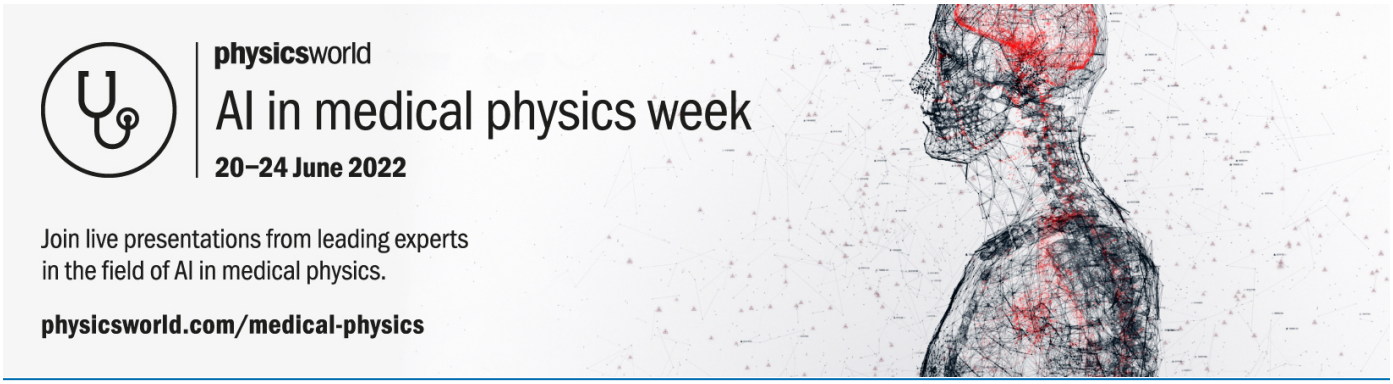

IOP Publishing Smart Materials and Structures
Smart Mater. Struct. **31** (2022) 075020 (16pp) https://doi.org/10.1088/1361-665X/ac7594

A toughening design for stretchable composite embedded with strain-rate stiffening elastomer

Chunyu Zhao, Yu Wang*, Mingyang Ni, Bochao Wang, Huaxia Deng*, Shouhu Xuan and Xinglong Gong*

CAS Key Laboratory of Mechanical Behavior and Design of Materials, Department of Modern Mechanics, University of Science and Technology of China, Hefei, Anhui 230027, People's Republic of China

E-mail: wyu@ustc.edu.cn, hxdeng@ustc.edu.cn and gongxl@ustc.edu.cn

Received 30 January 2022, revised 18 April 2022
Accepted for publication 1 June 2022
Published 15 June 2022

Abstract

Herein, a macroscopic double-network (DN) design for stretchable composite is proposed by embedding strain-rate stiffening elastomer (SSE) reinforced bars into the Ecoflex matrix. Due to the complementarity of mechanical properties between the soft-phase Ecoflex and hard-phase SSE as well as the strong interfacial bond strength, the Ecoflex/SSE composite achieves higher toughness and fatigue threshold than traditional single-network elastomers. Besides, based on the crack propagation characterization, strain-field evolution investigation, and finite element analysis, the fracture toughness of the Ecoflex/SSE composite is proved to be enhanced with the increase of the external strain rates. Interestingly, a sideway crack-arrest morphology is observed above 0.1 s^{-1}, displaying a better anti-crack ability of the Ecoflex/SSE composite at the higher strain rate. As a fundamental research in macroscopic DN composite, the method in this work provides a new idea for the toughening optimization of the strain-rate stiffening material. With the high fracture toughness, fatigue threshold, and flexibility, the Ecoflex/SSE composite has broad application prospects in designing high-performance stretchable elastomers.

Keywords: polymer-matrix composite, stretchable material, structural design, fracture toughness, strain-rate stiffening elastomer (SSE)

(Some figures may appear in colour only in the online journal)

1. Introduction

Stretchable materials, with low modulus and good flexibility, have shown broad application prospects in the fields of intelligent wearables [1–3], soft robots [4–6], stretchable electronics [7, 8], and drug deliveries [9, 10]. Nowadays, focusing on material synthesis [11, 12], structural design [13–15], and performance optimization [16, 17], researchers all over the world have made many contributions to optimize the material property. However, the load-bearing capacity and structural stability against the crack propagation for existing stretchable composites are relatively limited, which undeniably seriously restricts their development in practical applications [18]. Therefore, exploring feasible toughening methods to improve the crack resistance capability for stretchable materials, becomes a top priority.

Nowadays, researchers have proposed a series of optimization schemes from multi-scale levels to improve the mechanical performance of stretchable materials. At the microscopic scale, by introducing isotropically pre-stretched sacrificial bonds into an ethyl acrylate system, the stiffness and toughness of the modified composite can be significantly improved [19]. Similarly, King *et al* also propose a double-network

* Authors to whom any correspondence should be addressed.

(DN) method to optimize the mechanical behavior of polyacrylamide hydrogel using controllable physical sacrificial networks [20]. Moreover, due to the rapid development of additive manufacturing technology and the increasing understanding of the fracture mechanisms of heterogeneous materials, several attempts have been made to design high-performance stretchable architectures at the macroscopical scale [21–23]. Li *et al* report a fatigue-resistant elastomer with a fatigue threshold beyond 500 J m^{-2} by printing hard elastomer into the soft matrix [24]. Additionally, Xiang *et al* propose a general principle to fabricate the hydrogel-elastomer structure, which guides the research directions for the macroscopical DN composite [25].

In terms of practical engineering applications, the mechanical behavior of the stretchable composite is easily affected by the variation of external loading strain rates [26]. However, the existing toughening methods for the stretchable composite mainly focus on property optimization at a specific loading strain rate. There is still a lack of research on property optimization based on the strain rate-dependent effect. It is known that most stretchable elastomers exhibit either strain rate-independent or strain rate-weakened phenomena during the crack propagation process [27]. The bottle-neck issue seriously influenced the practicability of stretchable materials due to their limited fracture toughness and fatigue threshold with the increase of the external strain rates. Recently, strain-rate stiffening material, a kind of high macromolecule composed of boron-siloxane, is reported to possess an interesting strain-rate stiffening ability due to the dynamic physical crosslinking [28, 29]. The storage modulus of strain-rate stiffening materials can be significantly increased by improving external strain rates within a short response time [30, 31]. Therefore, it is a novel attempt to design a crack-resistance stretchable elastomer with strain-rate stiffening components.

Herein, a macroscopic DN structure was fabricated by embedding lattices of strain-rate stiffening elastomer (SSE) reinforcement bar into the Ecoflex soft matrix. Resulted from the coupling effect of the SSE and Ecoflex with discrepant modulus and good interfacial adhesion, the fracture toughness and fatigue threshold of the Ecoflex/SSE composite was improved effectively compared with other traditional elastomers. Besides, due to the unique mechanical behavior of SSE, the strain-rate stiffening effect was successfully combined with the toughening design of stretchable materials for the first time. The composite design method proposed in this paper can not only expand the application field for strain-rate stiffening materials but also promote the development of stretchable devices.

2. Materials and methods

2.1. Synthetic method for Ecoflex and SSE elastomer

The Ecoflex used in this paper was a commercial platinum-catalyzed elastomer (Ecoflex™ 00-20, purchased from Smooth-On, USA). Part A and part B of the Ecoflex precursor were manually mixed at the weight ratio of 1:1 for 5 min to obtain the unvulcanized Ecoflex. Afterward, the precursor solution was poured into the aluminum mold and degassed in a vacuum chamber until the bubbles were utterly removed. Subsequently, the mixture was vulcanized at 100 °C for 10 min to produce the final Ecoflex elastomer (figure 1(a)).

The mixture of boric acid (AR degree, purchased from Sinopharm Chemical Reagent Co. Ltd, Shanghai, China) and hydroxyl silicone oil (AR degree, purchased from Jining Huakai Resin Co., Ltd, China) were heated at 180 °C for 2 h in an oven to obtain the strain-rate stiffening gel (SSG) raw material (figure 1(b)). To fabricate the raw materials for the SSE, the same weight of as-prepared SSG and methyl vinyl silicone rubber (VMQ 110-2, purchased from Shenzhen Muwei Technology Co., Ltd) were stirred mechanically in an internal mixer (HL-200, Jilin University, China) at 45 rpm for 30 min. In the process of mixing, 1.0 % w.t. of benzoyl peroxide (BPO, CP degree, purchased from Sinopharm Chemical Reagent Co. Ltd, Shanghai, China) was dispersed into the SSG-VMQ mixture as the vulcanizing agent. Then, the mixture was vulcanized using a plate vulcanizer under 100 °C and 20 MPa for 15 min in the customized aluminum mold. Finally, the SSE with specific shapes could be obtained after the cooling and demolding (figure 1(c)).

2.2. Preparation process of the Ecoflex/SSE composite

The Ecoflex/SSE composite was composed of the Ecoflex matrix and SSE reinforcement bar. Firstly, an Ecoflex elastomer sheet with the dimension of 70 mm × 40 mm × 1 mm was placed into an aluminum mold of 70 mm × 40 mm × 3 mm as the bottom matrix of the composite. Secondly, the SSE reinforcement bars with the size of 5 mm × 40 mm × 1 mm were evenly distributed on the Ecoflex matrix with an interval of 5 mm. Afterward, the remaining space was filled with the unvulcanized Ecoflex precursor solution. Notably, the vulcanization process of Ecoflex/SSE was the same as that of Ecoflex except for the pressure. The pressure was set as 20 MPa to promote the interface bonding performance between the Ecoflex and SSE. Finally, the stretchable Ecoflex/SSE composite was obtained through a cooling and demolding process (figure 1(d)). From the SEM (SEM 500, Carl Zeiss Microscopy Ltd UK) image, the Ecoflex and SSE were in close contact at the interface region (figure A1).

2.3. Mechanical characterization

In order to evaluate the mechanical properties of Ecoflex/SSE composite, the uniaxial tension test, T-peeling test, crack propagation test, and cyclic fatigue test were conducted using a universal tensile instrument (Criterion™ Model 43, MTS Co., LTD, China) with a 500 N force sensor module.

For the uniaxial tension test of homogeneous Ecoflex and SSE, the specimen was cut into a rectangular shape with the effective size of 40 mm × 20 mm × 2 mm by a metal cutter (ISO 37:2017). During the stretching process, the length of the specimen was parallel to the loading direction, while the width was perpendicular to the loading direction. The rate-dependent

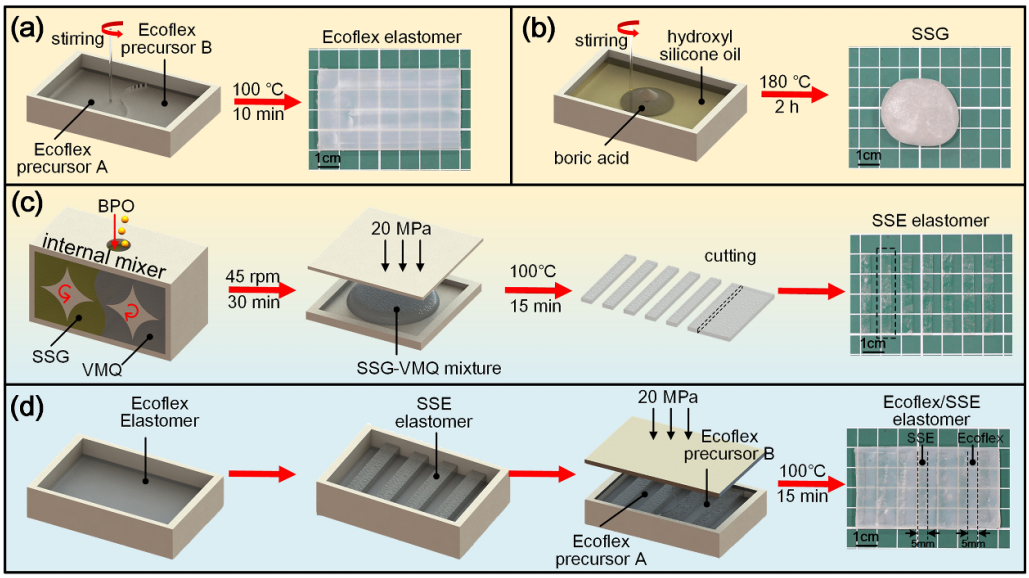

Figure 1. The preparation procedures for Ecoflex/SSE composite. (a)–(c) The synthesis of Ecoflex, SSG, and SSE. (d) The assembly of Ecoflex/SSE composite.

effect of the Ecoflex/SSE composite was investigated under the tensile strain rates of 0.01 s^{-1}, 0.1 s^{-1}, and 0.5 s^{-1}, respectively.

The T-peeling test was conducted to measure the interfacial adhesion between the Ecofelx and SSE. The SSE was primarily fabricated with a dimension of 60 mm × 20 mm × 2 mm and placed into a 60 mm × 20 mm × 4 mm aluminum mold. Secondly, a PET film (10 mm × 2 mm) was attached to the end of the SSE to form the initial crack. Then, the liquid Ecoflex precursor with the same volume as SSE was added into the mold. The whole specimen was put into a flat vulcanizer under an environment of 100 °C, 20 MPa for 15 min to form interfacial adhesion between the SSE and Ecoflex (ISO 11 339:2010). Besides, unpressurized specimens of the same geometric dimension were also prepared to explore the influence of pressurization on the interfacial properties of the Ecoflex/SSE composites. Furthermore, the PET films of 80 mm × 20 mm × 2 mm were pasted to the backsides for both SSE and Ecoflex using Sil-Poxy™ (purchased from Smooth-On, USA) silicone adhesive to restrain the deformation of the peeling arms. In the T-peeling test, the effective bonding area for the specimen was 50 mm × 20 mm, and the tensile rate was 0.4 mm s^{-1} and 4 mm s^{-1}.

For the Ecoflex/SSE composite, the notched specimen with an effective size of 70 mm × 20 mm × 3 mm was prepared by cutting a 15 mm initial crack from the midline of one side of the composite according to the principle proposed in the previous study [32]. The experimental parameters in the crack propagation test were the same as the uniaxial tensile test except for the specimen's geometry. It was worth mentioning that the black speckles were randomly sprayed on one surface of the sample in the undeformed state. In this case, the deformation history could be analyzed through the digital image correlation (DIC) method using a CCD camera (MV-CA050-11UM, Hikvision, China) with a calibrated linewidth of 27.84 μm. The strain fields were calculated using Ncorr software, an open-source 2D digital DIC MATLAB program widely used to analyze the material deformation [33]. Moreover, an ordinary digital camera (iPhone 7, 1080p HD, 60 fps) was placed perpendicularly to another specimen surface without the black speckles to record the deformation morphologies of the Ecoflex/SSE composite.

For the cyclic fatigue test of the Ecoflex/SSE composite, the dimension of the specimen was the same as that in the crack propagation test. Under the cyclic fatigue loading, the notched specimens were stretched from the undeformed state ($\lambda = 1$) to the amplitude value ($\lambda = \lambda_m$) and then unloaded to $\lambda = 1$ at the frequency of $f = 0.2$ Hz (ISO 9664:1993). According to the previous report, the fatigue threshold was defined as the number of cycles corresponding to the failure of the first SSE reinforcement bar in the crack propagation direction [25]. Moreover, the unnotched specimen was repeatedly stretched with the same experimental conditions as the notched one to calculate the energy release rate (G) based on the integral of the stress-stretch curve at the failure cycle (N). Meanwhile, the abovementioned DIC method was used to record the crack propagation process and identify the failure cycle for the Ecoflex/SSE specimen.

3. Results and discussion

3.1. The basic mechanical properties for Ecoflex, SSE, and Ecoflex/SSE interface

The uniaxial tension test of Ecoflex and SSE was primarily carried out to determine the mechanical properties of each component in the composite (figure 2(a)). The homogeneous Ecoflex exhibited a typical hyperelastic behavior

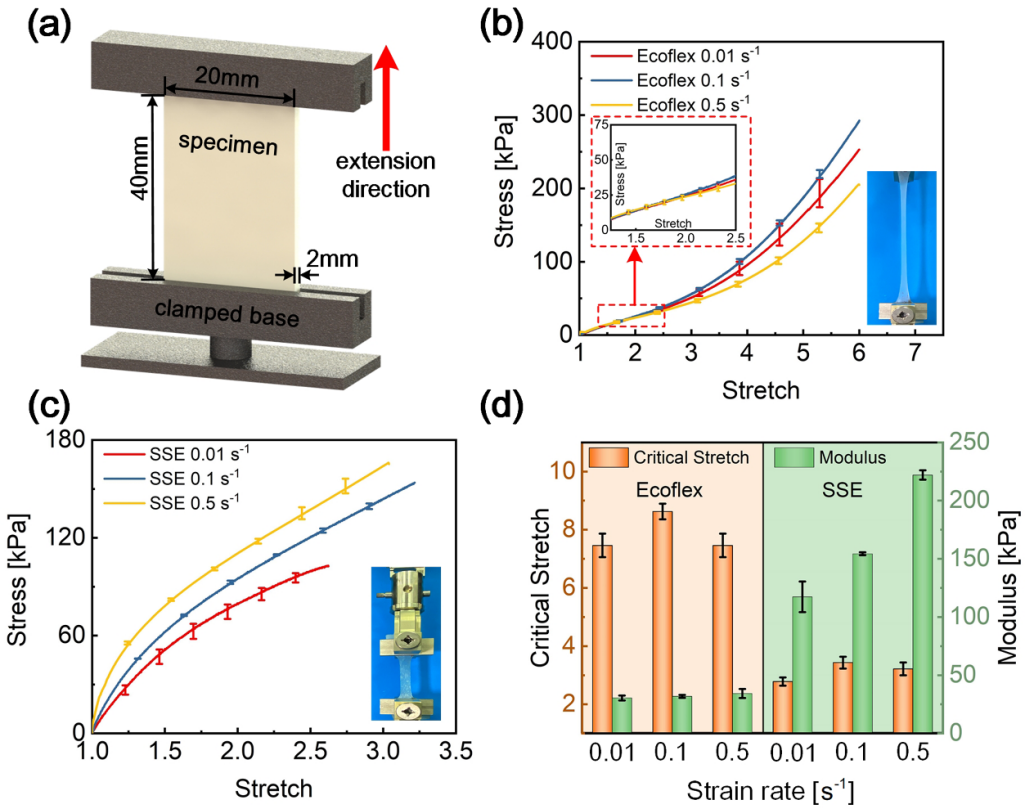

Figure 2. The uniaxial tensile test for Ecoflex and SSE elastomer. (a) The schematic of the uniaxial tensile test and the dimension of the specimen. (b) The stress vs. stretch curve of Ecoflex elastomer before $\lambda < 6$. (The insets are the partial enlarged detail between $\lambda = 1.25$–2.5 and the stretchability of Ecoflex before fracture) (c) The stress vs. stretch curve of SSE elastomer. (The inset is the stretchability of SSE before fracture) (d) The critical stretch and calculated modulus for Ecoflex and SSE (the modulus is defined as the secant modulus at the stretch of $\lambda_c = 1.25$). (Error bars: S.D., $n = 3$).

with a significant stretch value from the nominal stress vs. stretch curve. At a small elongation ratio, the stress level of Ecoflex was limited (14 kPa at $\lambda = 1.5$). However, with the increase in elongation ratio, the strain hardening effect appeared, and the Ecoflex could continue to sustain loading under large deformation. Additionally, the coincidence of the tensile curves ($\lambda < 3$) demonstrated that the mechanical behavior of the Ecoflex elastomer was almost rate-independent at the low stretch range (figure 2(b)). Unlike the hyperelastic Ecoflex, SSE was considered a classical viscoelastic material. The stress vs. stretch curve of SSE illustrated that the modulus of SSE increased with the growth of the loading strain rates (figure 2(c)). Besides, the SSE was stiffer than Ecoflex, with higher stress levels at the same stretch. (45–81 kPa at $\lambda = 1.5$). The rheological testing results further indicated the rate-dependent effect for SSE (figure A2). Based on the comparison of the mechanical behavior of Ecoflex and SSE, the Ecoflex matrix had a larger elongation ($\lambda > 7$). Meanwhile, the modulus of SSE was larger than the Ecoflex, with an interesting strain-rate stiffening effect (figure 2(d)).

The T-peeling test was conducted to characterize the adhesion strength of SSE and Ecoflex. An initial crack of 10 mm was introduced to the interface of the double-layer specimen in the preparation process (figure 3(a)). The peeling force vs. displacement curve was recorded by a force sensor in the universal tensile instrument during the T-peeling test. With the increase of the extension, the peeling force gradually reached a plateau region before the specimen was completely stripped. For the unpressurized specimens, the force value in the plateau region was far below the specimens with the pressurized specimen. Besides, the difference in adhesive property was more evident with the increase in peeling velocity between the unpressurized and pressurized specimens (figure 3(b)). The adhesion strength was defined as

$$\Gamma_p = 2P_m/w, \tag{1}$$

where the P_m is the average peeling force at the plateau, and the w is the width of the peeling specimen [34]. The adhesion strength for unpressurized specimens was only 70–85 J m^{-2}, while the adhesion strength for pressurized specimens was 122–343 J m^{-2}. The interface morphology between the Ecoflex and SSE was also recorded during the peeling process. For the specimen after pressurizing modification, there was an apparent bonding phenomenon between the interface when Ecoflex and SSE were separated. However, the bonding effect was feeble for the unpressurized specimens (figures 3(c) and (d)). Fourier transform infrared spectroscopy (FT-IR) could also indirectly prove the effect of pressurization on the interface of Ecoflex/SSE composites. Compared with the unpressurized specimens, the B–O absorption peak (which originally existed only in the SSE system) appeared in the

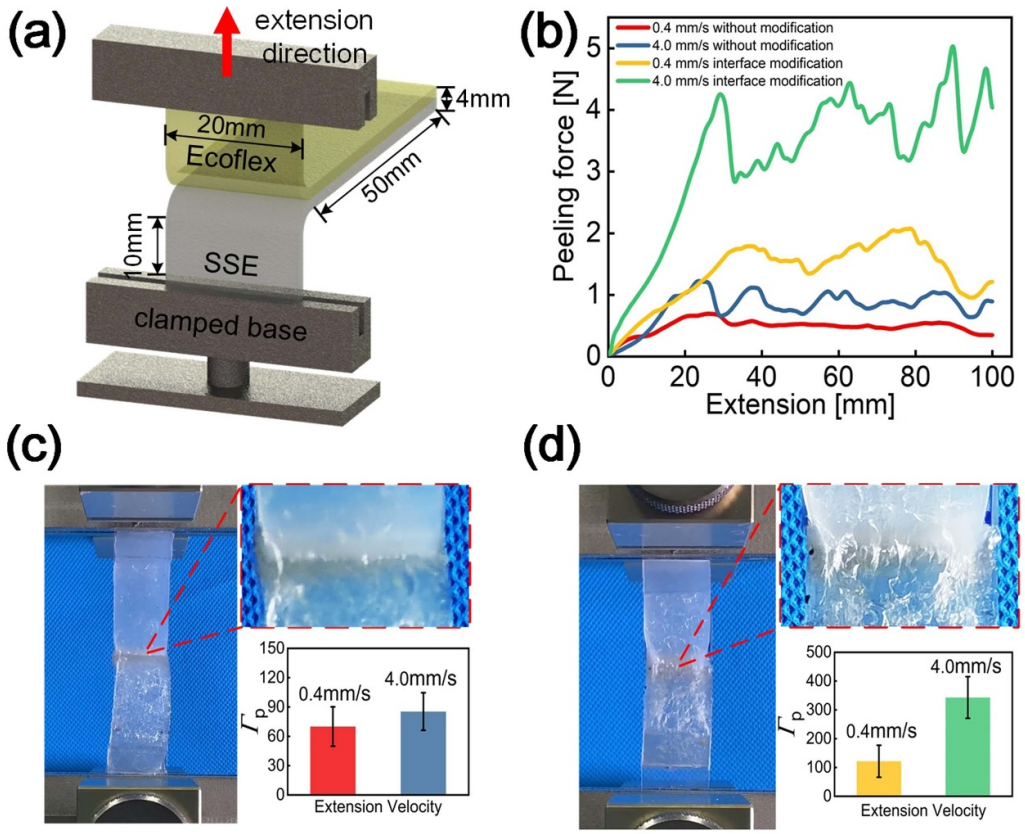

Figure 3. The T-peeling test for Ecoflex and SSE. (a) The schematic of the T-peeling test and the dimension of the specimen. (b) The peeling force vs. extension curve of the double-layer Ecoflex and SSE with different modification methods and extension velocities. (c) The interface topography of the unpressurized specimen and calculated peel strength. (d) The interface topography of the pressurized specimen and calculated peel strength. (Error bars: S.D., $n = 3$).

pressurized Ecoflex after peeling (figure A3). Therefore, it indicated that more SSE was attached to the Ecoflex surface during the peeling process, and the interfacial bonding was effectively improved. In this case, the pressurizing modification during the preparation process endowed the Ecoflex/SSE composite with a better interfacial property.

3.2. The toughening effect against crack propagation for Ecoflex/SSE composite

To evaluate the ability of Ecoflex/SSE composite in resisting crack propagation under different strain rates, the crack propagation tests for notched Ecoflex, SSE, and Ecoflex/SSE (uniformly-spaced Ecoflex and SSE with the width rate of 1:1) specimens were carried out at the tensile strain rates of 0.01 s^{-1}, 0.1 s^{-1}, and 0.5 s^{-1}, respectively (figure 4(a)). Further, the fracture toughness (Γ_c) was calculated by

$$\Gamma_c = h_0 W(\lambda_c) = h_0 \int_{\lambda=1}^{\lambda=\lambda_c} \sigma(\lambda)\,\mathrm{d}\lambda, \tag{2}$$

to quantitatively measure the resistance against crack propagation [25, 34]. Where h_0 is the height of the specimen and $\int_{\lambda=1}^{\lambda=\lambda_c} \sigma(\lambda)\,\mathrm{d}\lambda$ represents the integral of the curve of stress ($\sigma(\lambda)$) vs. stretch (λ) for the unnotched specimen from $\lambda = 1$ to $\lambda = \lambda_c$ with the same dimension as the notched specimen (figure 4(b)). Firstly, the differences in mechanical behaviors of Ecoflex, SSE, and Ecoflex/SSE composite were analyzed through the stress vs. stretch curves. It should be noted that the critical stretch (λ_c) for homogeneous Ecoflex and SSE corresponded to the elongation when the stress reached the maximum value, and the λ_c for Ecoflex/SSE structure was defined as the stretch when the first SSE reinforcement bar broke [24]. Before reaching the λ_c value, the stress vs. stretch curves for notched Ecoflex specimens were almost coincident, displaying a rate-independent property. Differently, the tensile curves of notched SSE specimens exhibited a typical strain-rate enhanced effect. Due to the existence of the SSE reinforcement bar, the Ecoflex/SSE also displayed a similar strain rate-dependent behavior (figure 4(c)). The experimental results illustrated that there was little difference between the λ_c values for both notched homogeneous Ecoflex and Ecoflex/SSE under different strain rates ($\lambda_c = 2.5$–3.0), higher than that of the homogeneous SSE ($\lambda_c < 1.8$) (figure 4(d)). In this case, the Ecoflex matrix positively influenced the structural stability of the Ecoflex/SSE composite under large deformation. Besides, benefitting from the rate-dependent reinforcement effect of hard bar SSE, the secant modulus of Ecoflex/SSE showed a strain-rate stiffening behavior from 38 kPa at 0.01 s^{-1}, 51 kPa at 0.1 s^{-1}, and 65 kPa at 0.5 s^{-1}. It displayed a larger value than the homogeneous Ecoflex

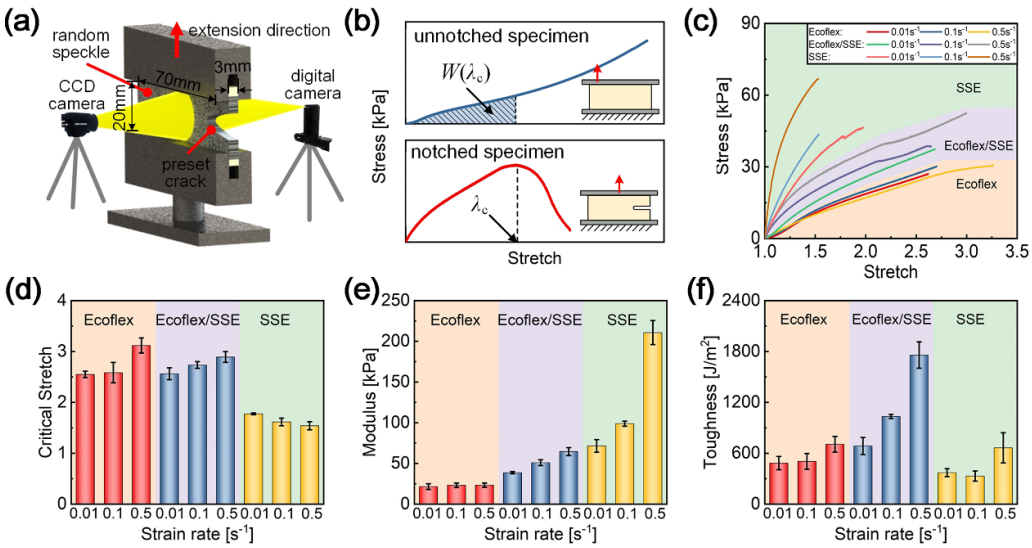

Figure 4. The mechanical behavior for notched homogeneous Ecoflex, SSE, and Ecoflex/SSE composite before crack propagation. (a) The schematic of the crack propagation test and the dimension of the notched specimen. (b) The definition of fracture toughness Γ_c. (c) The stress vs. stretch curve for homogeneous Ecoflex, SSE, and Ecoflex/SSE at different strain rates during the crack propagation before the λ_c value. (d)–(f) The calculated critical stretch, modulus, and fracture toughness for homogeneous Ecoflex, SSE, and Ecoflex/SSE at different strain rates. (The modulus is defined as the secant modulus at the stretch of $\lambda_c = 1.25$. Error bars: S.D., $n = 3$).

(22 kPa at 0.01 s^{-1}, 23 kPa at 0.1 s^{-1}, and 23 kPa at 0.5 s^{-1}) (figure 4(e)). In terms of the toughness, for the homogeneous Ecoflex, the calculated Γ_c value was not sensitive to the variation of strain rates among 504–705 J m^{-2} at different strain rates, while the Γ_c values for homogeneous SSE were relatively limited (370 J m^{-2} at 0.01 s^{-1}, 331 J m^{-2} at 0.1 s^{-1}, and 663 J m^{-2} at 0.5 s^{-1}). Unlike some fiber-reinforced polymer composites, whose fracture toughness was either rate-independent or rate-weakened [27, 35], the calculated Γ_c for the Ecoflex/SSE composite in this paper increased from 685 J m^{-2} to 1758 J m^{-2} with the growth of the tensile strain rates (figure 4(f)). Besides, the influence of SSE content on the mechanical behavior of the Ecoflex/SSE composite was also compared by changing the geometric dimensions of Ecoflex and SSE (figure A4). All of the tested specimens showed higher critical stretch values than the homogeneous SSE, which further verified the positive effect of the Ecoflex matrix on the integrity of Ecoflex/SSE composite against the crack propagation. Moreover, the uniformly-spaced Ecoflex and SSE with the width rate of 1:1 displayed the highest fracture toughness among all of the specimen at different strain rates. Therefore, this specimen were used to design the Ecoflex/SSE composite in the work as described in section 2.

In crack propagation, the evolutions of crack morphology corresponded to the specific mechanical behavior of materials. Generally, the crack tip opening displacement (CTOD) was used to characterize the crack behavior from the aspect of morphology [36–38]. In this paper, the CTOD was extracted from the images recorded by the CCD camera. The crack tip displacement (Dis_{crack}) and crack tip velocity (v_{crack}) were obtained by pixel recognition technology based on the CTOD data. For the homogeneous Ecoflex, a large amount of deformation energy was stored at the crack tip before the stress increased to the critical value (Stage I) [34]. Considering the isotropic character of Ecoflex elastomer, the opening mode crack (Mode I cracking) was observed in the crack propagation process. The Dis_{crack} increased rapidly, and the stress value at this stage quickly decreased due to the continuous destruction of the Ecoflex structure. Finally, the crack propagated at the edge part of Ecoflex, and the whole elastomer failed with penetrating the crack (Stage II). Additionally, the crack morphologies for two feature points were extracted, corresponding to the stage of crack initiation (point 1) and steady propagation (point 2), respectively. It should be noted that the crack shapes of the two feature points are highly similar and can be described by a power-law equation $x = y^n$ at all of the tensile rates, showing a no-inertia nature during the crack movements [39] (figures 5(a)–(c) and A5(a)–(c)).

The crack evolution was quite different for the Ecoflex/SSE composite. At the tensile rate of 0.01 s^{-1}, the Ecoflex/SSE gradually reached the λ_c value when the first SSE reinforcement bar failed (Stage I). The crack could continue to propagate into the Ecoflex network during the crack propagation process until the SSE reinforcement bar was destroyed. Due to the existence of reinforcement bar SSE, the penetration tendency of the crack tip was slightly alleviated. The Dis_{crack} stepwise increased to the maximum value rather than rapidly penetrating the homogeneous Ecoflex. Correspondingly, the gradual decay of stress value displayed in the stress vs. stretch curve with the alternative failure between the SSE and Ecoflex. Finally, a penetrating crack was observed once the whole composite was destroyed (Stage II). Under the circumstances, the crack blunting phenomenon appeared, and the crack velocity displayed a fluctuant tendency. In this section, another two feature points were chosen to compare the CTOD at the different stages in crack propagation. Point 1 corresponded to the crack

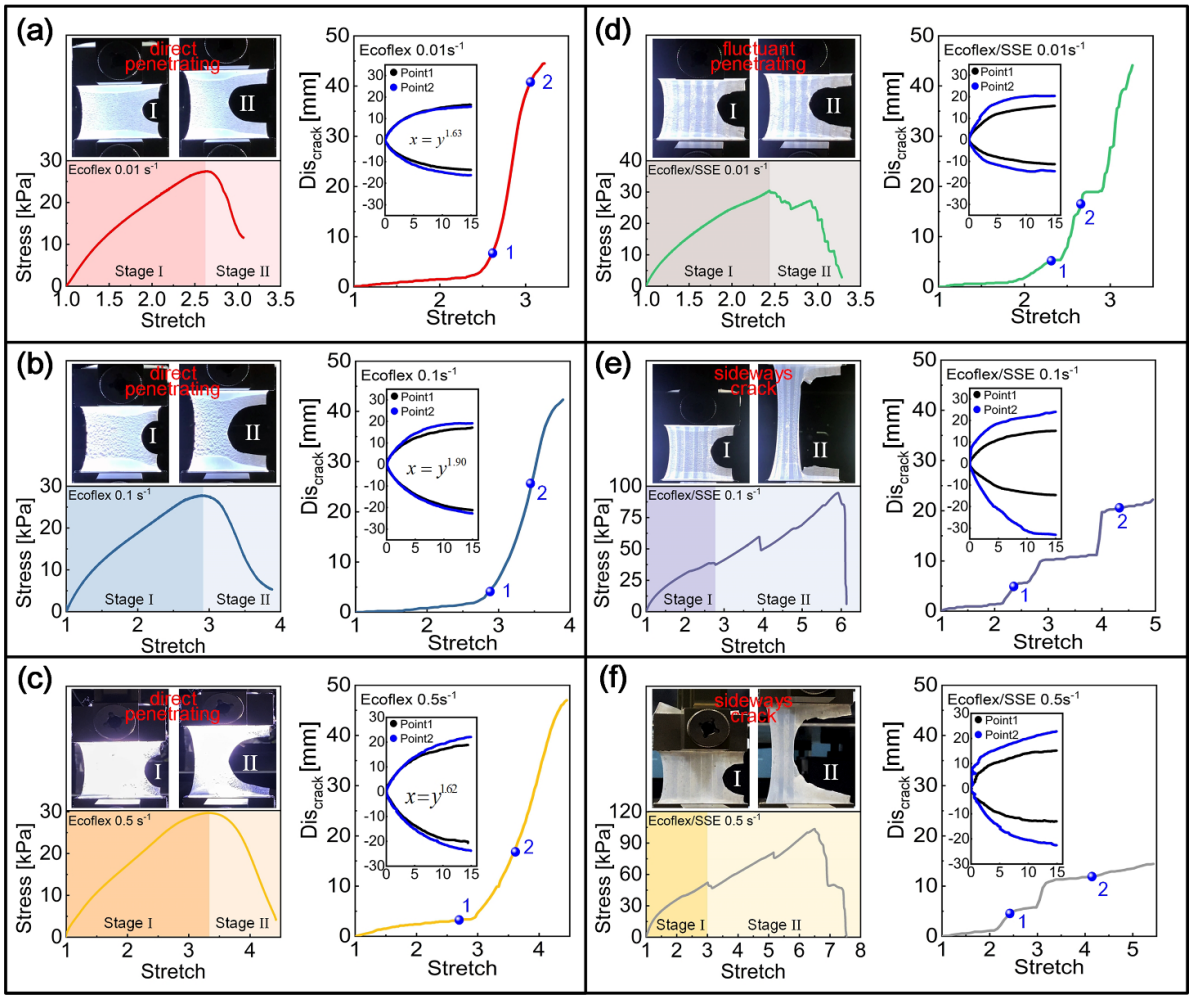

Figure 5. The comparison of crack propagation process under different strain rates for the homogeneous Ecoflex and Ecoflex/SSE. (a)–(c) Homogeneous Ecoflex at the strain rate of 0.01 s^{-1}, 0.1 s^{-1}, and 0.5 s^{-1}; (d)–(f) Ecoflex/SSE at the strain rate of 0.01 s^{-1}, 0.1 s^{-1}, and 0.5 s^{-1}. (The first column is the stress vs. stretch curve and corresponding morphology evolutions during the crack propagation. The second column is the crack displacement vs. stretch curve, and the inset is the CTOD of the feature points, respectively).

initiation, and point 2 corresponded to the keyframe when the crack tip was blunted at the interface. It was illustrated that the crack opening angle of point 2 was more significant than point 1. The previous report showed that a larger crack opening angle represented the more strain energy accumulated in the crack tip region [40, 41]. Therefore, more energy was needed to drive the crack tip movement, which improved the fracture toughness of the Ecoflex/SSE composites.

At higher strain rates of 0.1 and 0.5 s^{-1}, the toughness of Ecoflex/SSE was enhanced due to the strain-rate stiffening effect. Interestingly, the fracture evolution still showed a penetrating style at the initial crack propagation stage (Stage I). However, a sideways crack was captured at the interface of Ecoflex and SSE with the growth of the crack tip (Stage II). Under this circumstance, the crack tip was effectively arrested, proven by a longer plateau region in crack growth vs. stretch curve. The region ahead of the crack front continued to sustain the tensile loadings even at large λ values. Finally, the Ecoflex/SSE composite achieved higher stretchability and maximum stress value before the crack propagated to the end of the clamping end. Similarly, the CTODs of two keyframes were extracted when the crack started to propagate (point 1) and the crack tip was arrested (point 2), respectively. Compared with the experimental results at 0.01 s^{-1}, the contrast of crack opening angles between point 1 and point 2 at 0. 1 s^{-1} and 0.5 s^{-1} were more prominent, indicating more accumulation of strain energy at the crack tip region (figures 5(e), (f), A5(e) and (f)).

The Lagrange strain fields in the y-direction (ε_{yy}) for the homogeneous Ecoflex and Ecoflex/SSE in the crack propagation process were calculated by Ncorr software [33]. In the strain field contours, the red region with the high ε_{yy} value represented the crack tip position, while the movement of the red region corresponded to the crack propagation. At the strain rate of 0.01 s^{-1}, four feature points with a strain interval of 0.06 were selected to analyze the evolution rules of the crack growth. For the homogeneous Ecoflex, the crack tip started to move when the high strain region ε_{yy} accumulated to

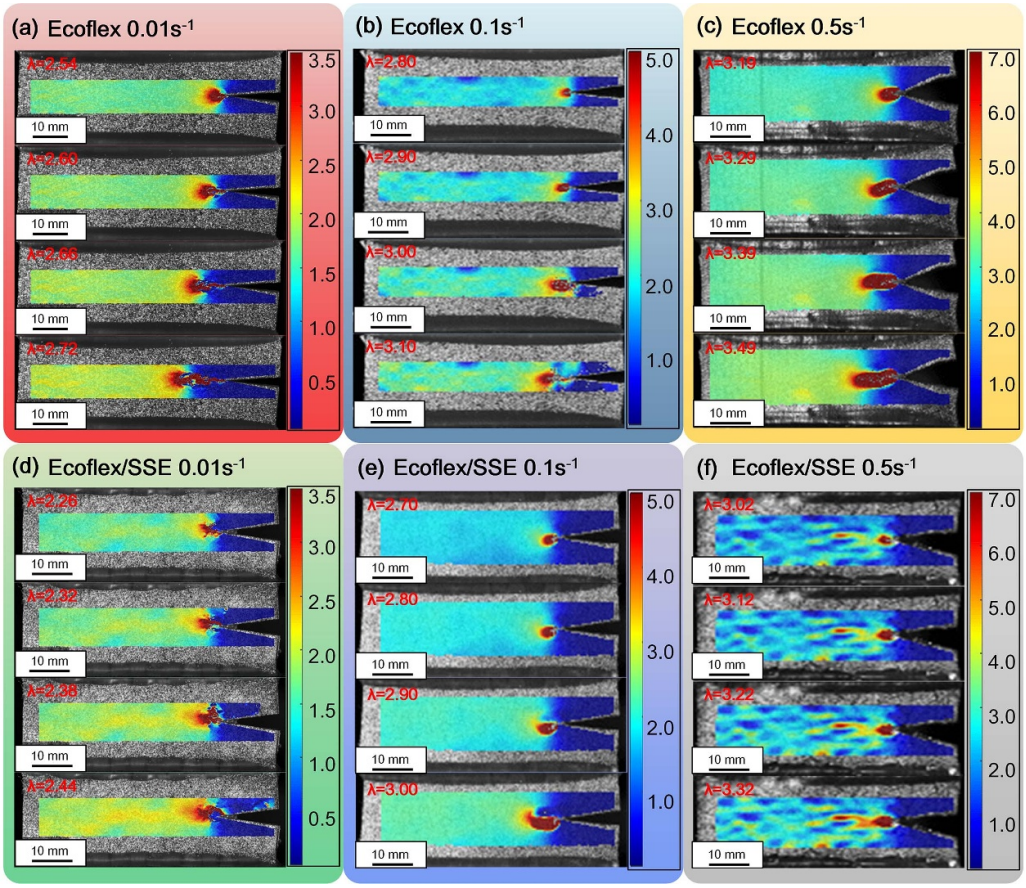

Figure 6. The Lagrange strain ε_{yy} contour for different feature points when the crack tip started to grow in the crack propagation process. (a)–(c) Homogeneous Ecoflex at 0.01 s^{-1}, 0.1 s^{-1}, and 0.5 s^{-1}. (d)–(f) Ecoflex/SSE at 0.01 s^{-1}, 0.1 s^{-1}, and 0.5 s^{-1}.

a critical extent. Once crack growth occurred, the crack tip propagated promptly, proved by the movement of the symmetrical red high strain region (figures 6(a)–(c)). For the Ecoflex/SSE, the crack tip movement with a high ε_{yy} value was limited after contact with the reinforcement bar SSE, which indicated that the existence of SSE could restrict the crack growth. Compared with the homogeneous Ecoflex, a more high strain region occurred at the crack tip of Ecoflex/SSE. Therefore, more energy accumulated at the crack tip before the crack continued to propagate, leading to the toughness enhancement from a macroscopic perspective (figure 6(d)). At the strain rate of 0.1 s^{-1} and 0.5 s^{-1}, another four feature points with a strain interval of 0.10 were also recorded to compare the crack behavior of homogeneous Ecoflex and Ecoflex/SSE. Similarly, the Ecoflex/SSE composite could effectively limit the movement of the high strain crack tip against the crack propagation, which further proved the anti-fracture property of the SSE reinforcement bar (figures 6(e) and (f)).

The finite element analysis (FEA) method was also used to explain the toughening effect of Ecoflex/SSE based on the Abaqus/Standard module. The notched Ecoflex and Ecoflex/SSE composite were assumed to satisfy the plane stress assumption to improve the convergence of the calculation results, using a four-node bilinear plane stress quadrilateral element. The Ecoflex and Ecoflex/SSE geometries were simplified as 70 mm × 20 mm thin sheets with a 15 mm initial crack. The spacing between two adjacent SSE reinforcement bars was 5 mm. In the modeling process, all of the rotation and displacements were constrained at the fixed end. At the moving end, only the displacement in the X-axis and rotation were constrained. In this case, the specimens could be stretched at the specific velocities along the Y-axis.

In terms of the material parameters, a generalized Neo-Hookean (GNH) constitutive equation could well describe hyperelastic behavior for the homogeneous Ecoflex based on the UHYPER subroutine

$$\Phi = \frac{\mu}{2b}\left\{\left[1+\frac{b}{2}(I_1-3)\right]^2-1\right\}, \tag{3}$$

where Φ is the strain energy density function and I_1 is the quadratic sum of the three principal stretches. μ and b are material parameters representing the shear modulus at infinitesimal strain and the onset of strain stiffening, respectively [42, 43] (figure 7(a)). Besides, the viscoelastic behavior for SSE could be described by a standard linear solid (SLS) model, composed of a Kelvin element and a spring in series utilizing the UMAT subroutine [44]

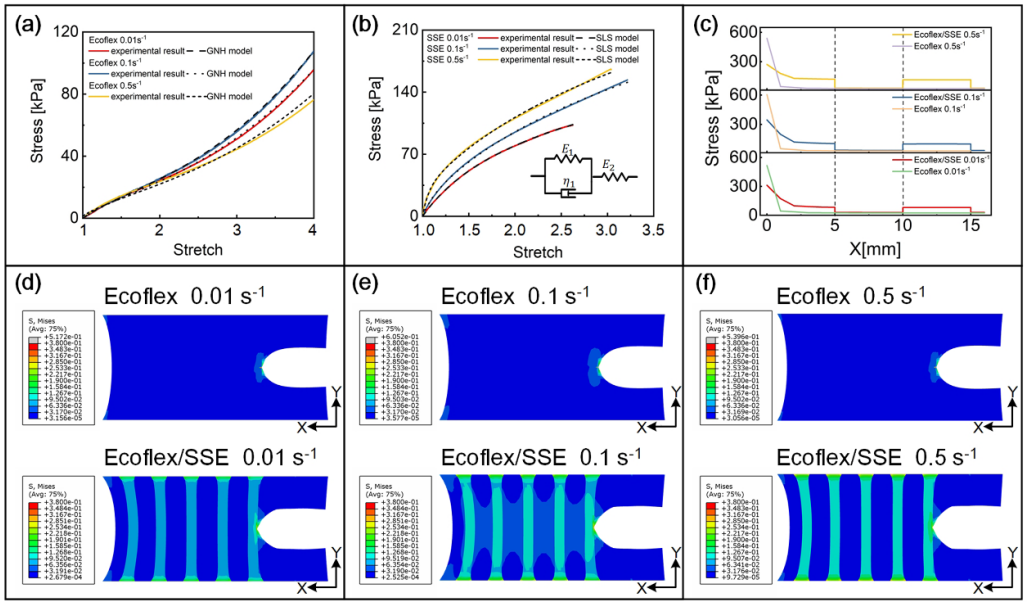

Figure 7. The FEA comparison of the ability against the crack tip for homogeneous Ecoflex and Ecoflex/SSE. (a) The fitting results for hyperelastic Ecoflex based on the generalized Neo-Hookean (GNH) model; (b) the fitting results for viscoelastic SSE based on the standard linear solid (SLS) model (the inset represents the SLS model); (c) the stress distributions along the X-axis for the homogeneous Ecoflex and Ecoflex/SSE at 0.01 s^{-1}, 0.1 s^{-1}, and 0.5 s^{-1}. (d)–(f) The comparison of full-field stress distributions for the homogeneous Ecoflex and Ecoflex/SSE at 0.01 s^{-1}, 0.1 s^{-1}, and 0.5 s^{-1}.

$$\sigma + \frac{\eta_1}{E_1 + E_2}\dot{\sigma} = \frac{E_1 E_2}{E_1 + E_2}\varepsilon + \frac{E_2 \eta_1}{E_1 + E_2}\dot{\varepsilon}. \tag{4}$$

Under the condition of uniaxial tension with a constant strain rate, there was an analytical solution to the above equation

$$\sigma = \frac{E_1 E_2}{E_1 + E_2}\varepsilon + \frac{E_2^2}{E_1 + E_2}\tau\dot{\varepsilon}\left(1 - e^{-\varepsilon/\dot{\varepsilon}\tau}\right), \tag{5}$$

where the σ is the stress, $\dot{\sigma}$ is the derivative of stress versus time, ε is the strain, and $\dot{\varepsilon}$ is the strain rate. E_1, E_2, and η_1 are the undetermined parameters in the SLS model, representing the elastic moduli for two springs and the viscosity for the dashpot, respectively. Additionally, $\tau = \eta_1/(E_1 + E_2)$ represents the characteristic time (figure 7(b)). For simplicity, the parameters for FEA were shown in table A1.

To investigate the influence of SSE on crack tip behavior, the process before the crack propagation from $\lambda = 1$ to $\lambda = 1.5$ was simulated. It was illustrated that the uniaxial tensile FEA simulation results of Ecoflex and SSE elastomers were in good agreement with the experimental results in the testing stretch range, which further proved the validity of the GNH model and the SLS model (figure A6). For the homogeneous Ecoflex, only the crack tip region was highly stretched before the crack propagation, while the Ecoflex in the far-field was insensitive to the evolution of the cracks tip. The stress concentration at the crack tip was apparent, which was easy to initiate crack propagation. Moreover, the stress states near the crack tip were almost the same at different strain rates in the numerical simulation, which further verified the rate-independent behavior of the homogeneous Ecoflex. For the Ecoflex/SSE composite, the SSE with a high modulus could dissipate more strain energy at the same elongation, resulting from the modulus differences between the SSE reinforcement bars and Ecoflex matrix. Besides, the bonding effect generated more shearing force in the interface of Ecoflex and SSE. Based on the synergistic effect of Ecoflex and SSE, more regions at the crack tip were involved in resisting crack propagation. The stress concentration phenomenon was effectively alleviated. Compared with the homogeneous Ecoflex, it was illustrated that the SSE reinforcement bar in the far-field also displayed a higher stress level in Ecoflex/SSE composite. As the increment of strain rates, the stress value of far-field SSE was enhanced due to the strain-rate stiffening effect. In this case, more strain energy was required for crack initiation, and the Ecoflex/SSE showed an improved anti-crack property at the macro-level (figures 7(c)–(f)).

3.3. *Fatigue behavior of Ecoflex/SSE structure*

The fatigue threshold was also an essential mechanics index to measure the durability of stretchable materials in practical applications. The cyclic tensile test was conducted to study the fatigue behavior of the Ecoflex/SSE composite using the same dimension in the crack propagation test. During the cyclic test, the various energy release rates (G) could be obtained by changing the stretch amplitude (figure 8(a)). According to the previous report [25], the failure cycle (N) corresponded to the cyclic number when the crack penetrated the first reinforcement bar in the Ecoflex/SSE. The N values were controlled extensively from 10^0 to 10^4 to illustrate the fatigue response better. In this paper, the fatigue threshold Γ_0 is defined as the energy release rate when $N > 10^4$. Under the higher energy release

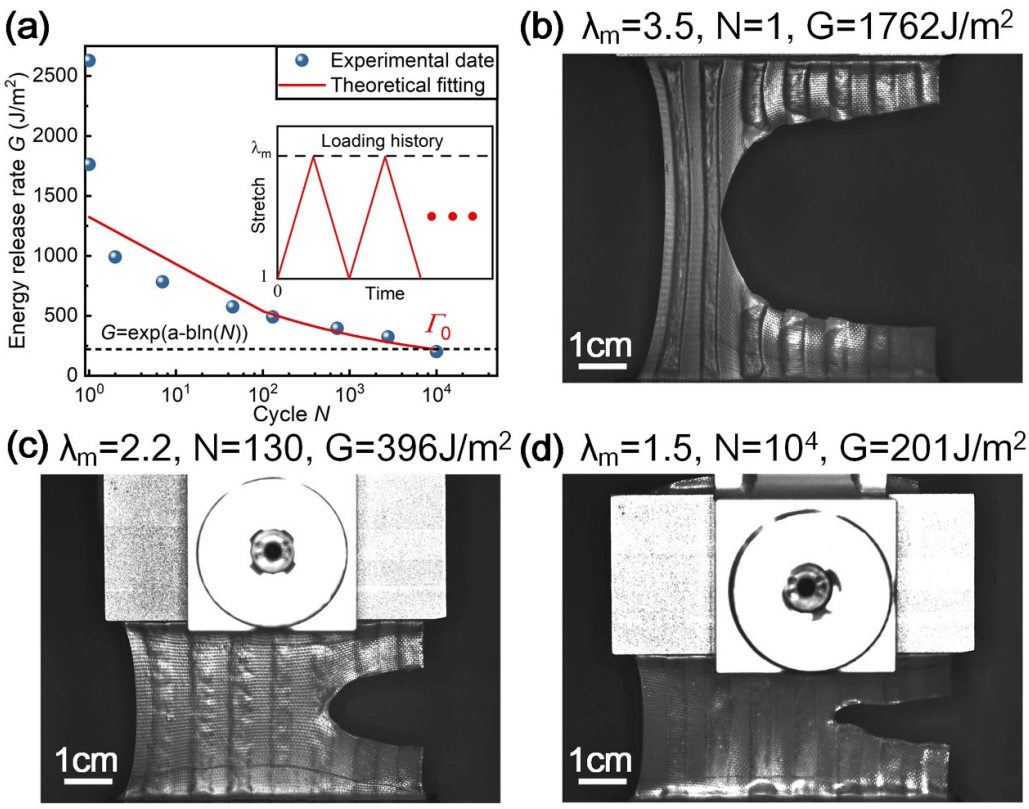

Figure 8. The fatigue behavior for Ecoflex/SSE composite. (a) The *G*–*N* curve of the Ecoflex/SSE composite (the inset represents the cyclic loading history); (b) the snapshot of the failure process for Ecoflex/SSE at $N = 1$ subjected to the stretch amplitude of 3.5 and energy release rate of 1762 J m^{-2}; (c) the snapshot of the failure process for Ecoflex/SSE at $N = 130$ subjected to the stretch amplitude of 2.2 and energy release rate of 396 J m^{-2}; (d) the snapshot of the crack arrest for Ecoflex/SSE at $N = 10^4$ subjected to the stretch amplitude of 1.5 and energy release rate of 201 J m^{-2}.

rate ($G > 1762$ J m^{-2}), the composite completely failed in the first cycle, with a large amount of strain energy released by the fracture of SSE (figure 8(b)). With the decrease of energy release rate, the Ecoflex/SSE could maintain the structural integrity under more cycles of the loading and unloading process. The crack tip penetrated only one SSE reinforcement bar at $N = 130$ when the energy release rate decreased to $G = 396$ J m^{-2} (figure 8(c)). Further, the crack tip was stopped by the SSE reinforcement bar at a lower energy release rate of $G = 201$ J m^{-2} over 10^4 cyclic (figure 8(d)). The relationship between the G and N accorded with the following classical fatigue experimental theory $G = e^{m-n\ln(N)}$, where m and n were the undetermined parameters [24]. The asymptotic line of the G vs. N curve was identified as the fatigue threshold of the Ecoflex/SSE composite with $\Gamma_0 = 201$ J m^{-2}.

The experimental results of the crack propagation test and cyclic fatigue test indicated that the Ecoflex/SSE elastomer achieved the balance of fracture toughness and fatigue threshold. It was reported that the existing elastomer materials often possessed high toughness (10^3–10^5 J m^{-2}), while the corresponding fatigue threshold was very low (below 10^2 J m^{-2}), which undeniably affected the long-term usability of the material [34, 45–47]. The Ecoflex/SSE composite in this paper could effectively improve the fatigue threshold while achieving high toughness (figure 9(a)). Besides, compared with traditional PDMS elastomer materials, the Ecoflex/SSE composites also maintained a lower modulus [48] (figure 9(b)). Therefore, the stretchable elastomer with soft matrix and hard reinforcement bar provided a new concept for designing the high-performance strain-rate stiffening composite.

3.4. Toughening mechanism for the Ecoflex/SSE composite

Based on the above discussions, the toughening effect for the Ecoflex/SSE could be explained by the synergistic effect of Ecoflex and SSE. The Ecoflex matrix with low modulus and high stretchability ensured the overall ductility and flexibility of the composite. Besides, the SSE reinforcement bar with a higher modulus optimized the mechanical behavior and introduced a new energy dissipation mechanism. Moreover, the strong interactions between the matrix and reinforcement bar could maintain the integrity of the composite under large deformation. This concept for stretchable elastomers was consistent with the optimization method proposed in recent reports [24, 36], which further verified the applicability of this method in different material systems.

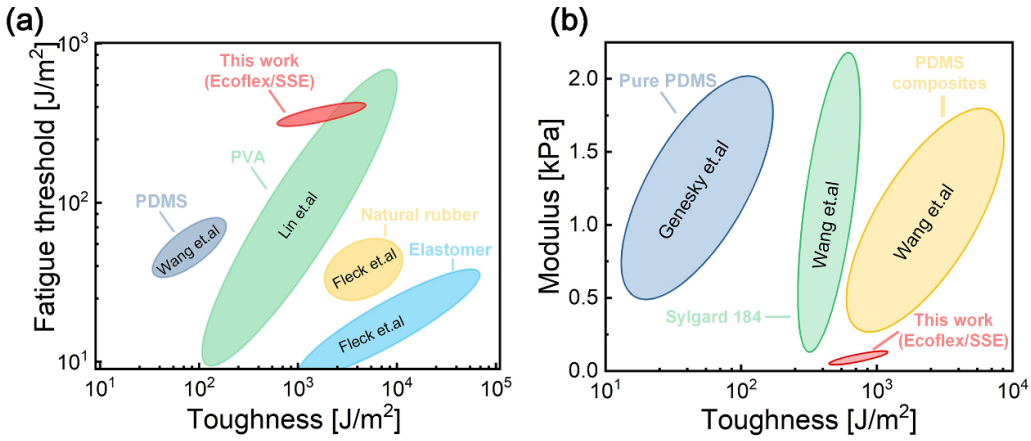

Figure 9. The comparison of mechanical properties between Ecoflex/SSE composite and other stretchable elastomers. (a) The comparison of the toughness and fatigue threshold between the different reported elastomers. (b) The comparison of the toughness and modulus between the different reported elastomers [34, 45–48].

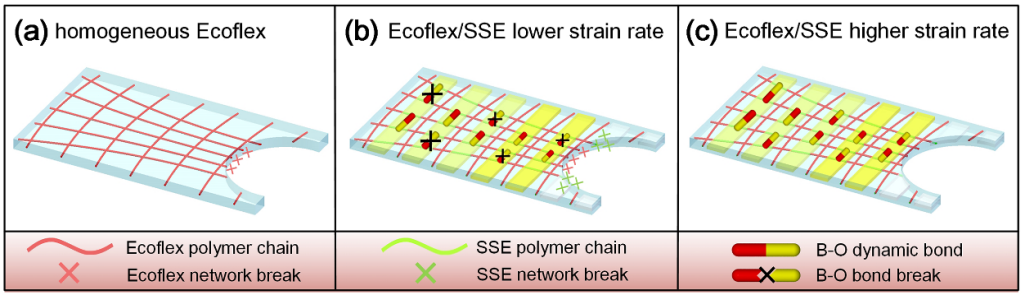

Figure 10. The microcosmic mechanism against crack propagation. (a) Homogeneous Ecoflex. (b) Ecoflex/SSE at lower strain rate of 0.01 s^{-1}. (c) Ecoflex/SSE at a higher strain rate above 0.01 s^{-1}.

From a microscopic point of view, for most single network polymer systems, the crack could easily break the single layer of molecular chains in the crack tip region [40]. Therefore, the homogeneous Ecoflex exhibited low fracture toughness during the crack propagation due to the limited energy dissipation (figure 10(a)). For the Ecoflex/SSE composite, an adhesion force generated at the interface between the Ecoflex and SSE resulted from the interpenetration effect of molecular chains. Before the crack started propagating, the Ecoflex matrix was highly sheared in the crack tip region. Due to the bonding effect at the interface, the SSE reinforcing bar could further elongate, accompanied by the deformation of the matrix material. The strain energy was not only released from the damage of molecular chains in the Ecoflex matrix. Benefitting from the high modulus of SSE, another significant part of the strain energy could also be released through the fracture of the SSE reinforcing bar. In this case, the fracture toughness of the Ecoflex/SSE structure was effectively enhanced (figure 10(b)).

Besides, the rate-dependent toughness behavior for Ecoflex/SSE composite could be described by the dynamic evolutions of boron–oxygen (B–O) physical crosslinking. Previous studies demonstrated that the B–O bond was easy to break with a characteristic time scale (τ_{b-o}) of about 10°s [49, 50]. Meanwhile, the loading characteristic time (τ_{load}) was defined as $\tau_{load} = \eta_1/(E_1 + E_2)$ based on the SLS model. Based on the analysis results from table A1, the calculated τ_{load} was 55.06 s, 0.95 s, and 0.12 s at the strain rate of 0.01 s^{-1}, 0.1 s^{-1}, and 0.5 s^{-1}, respectively. At lower frequencies, since the loading characteristic time τ_{load} was much longer than the τ_{b-o} of the B–O bond, the B–O bond has enough time to break. Under the circumstance, the molecular chains were disentangled and the polymer system showed a low modulus at the macro level. With the increment of frequency, the τ_{load} became less than the τ_{b-o}, more B–O bonds in the polymer system could not break, and the disentanglement effect was inhibited, which seriously hindered the movement of the molecular chains. The modulus of material increases and the polymer system displayed a highly elastic state, leading to a more remarkable difference in modulus between the SSE and Ecoflex. More strain energy was stored in the SSE segment before crack initiation, and the Ecoflex/SSE showed a higher toughness on a macroscale (figure 10(c)).

4. Conclusions

In this paper, a novel stretchable Ecoflex/SSE composite was designed based on the Ecoflex matrix and SSE reinforcement bar. The influence of the strain-rate effect of

SSE reinforcement bars on the fracture toughness of the Ecoflex/SSE composite was detailedly studied based on experimental investigation and finite element analysis. The conclusions are as follows.

- The Ecoflex/SSE composite achieved higher fracture toughness and fatigue threshold in comparison to the traditional single-network elastomers due to the complementarity of mechanical properties between the soft-phase Ecoflex and hard-phase SSE reinforcement bars as well as the strong interfacial bond strength.
- With the increase of external loading strain rates, the modulus of the SSE reinforcement bars improved due to the unique strain-rate stiffening effect. Therefore, the Ecoflex/SSE composite could dissipate more strain energy against the crack propagation, resulting in the improvement of fracture toughness of the material system.
- With the increase of external loading strain rates, a sideway crack-arrest morphology was observed above 0.1 s^{-1}. Under this circumstance, the movement of the crack tip was further arrested and the Ecoflex/SSE composite achieved higher stretchability as well as maximum stress value.
- The strain rate-dependent stiffening mechanism of composites could be explained by the finite element analysis and B–O bonds dynamic evolution.

As fundamental research in macroscopic DN material, the method proposed in this work effectively optimized the toughness and fatigue properties of the stretchable elastomers. The unique strain-rate stiffening toughening effect in Ecoflex/SSE composite is similar to the function of the ligamentous tissue in certain organisms. Therefore, the Ecoflex/SSE composite is a good candidate to fabricate a high-performance bionic structure for potential applications in soft robots and flexible electronic skin. Moreover, based on the developing additive manufacturing technology, it is also hoped that the Ecoflex/SSE composite with more complex SSE patterns and controllable mechanical properties can be realized in future work.

Data availability statement

All data that support the findings of this study are included within the article (and any supplementary files).

Acknowledgments

Financial supports from the National Natural Science Foundation of China (Grant Nos. 11972337, 12132016, and 11972032) are gratefully acknowledged.

Appendix

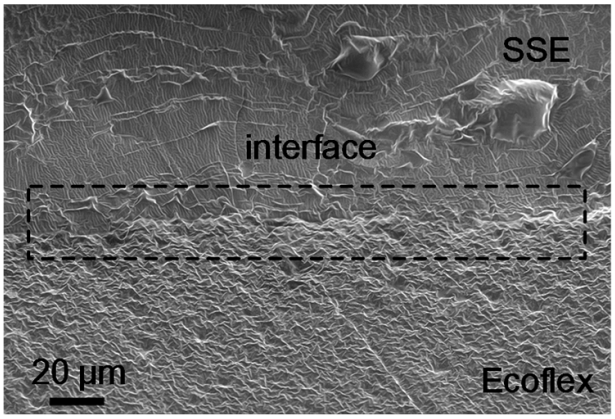

Figure A1. The SEM image of the interface between the Ecoflex and SSE.

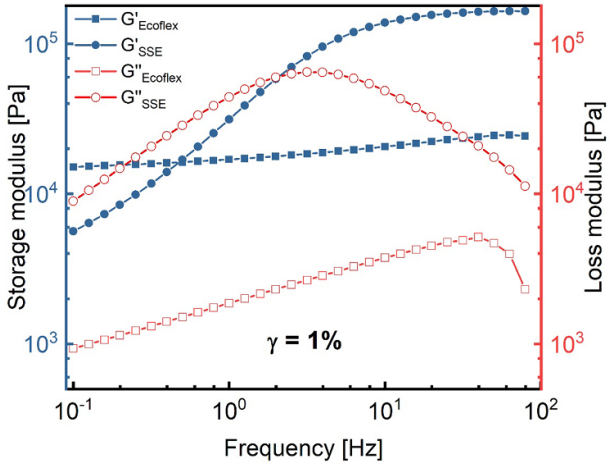

Figure A2. The rheological test results for SSE and Ecoflex. (The rheological properties of the homogeneous Ecoflex and strain-rate stiffening elastomer were studied by a rheometer (Physica MCR 302, Anton Paar Co., Austria), with the PP20 parallel plate (Φ20 mm). During the test, the specimen (Φ20 mm × 1 mm) was sheared by the plate using the oscillatory sweeping module at the temperature of 25 °C with an amplitude strain of 1%. The storage modulus (G') and loss modulus (G'') were recorded according to the frequency increment from 0.1 Hz to 100 Hz.).

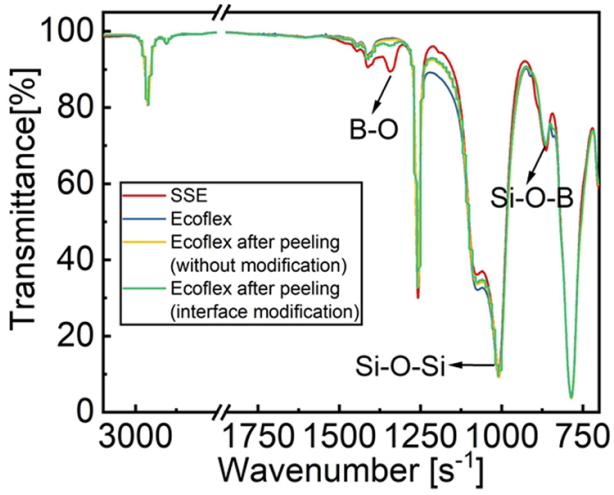

Figure A3. The comparison of FTIR (Fourier transform infrared spectroscopy) of SSE, Ecoflex, unpressurized Ecoflex after T-peeling, and pressurized Ecoflex after T-peeling.

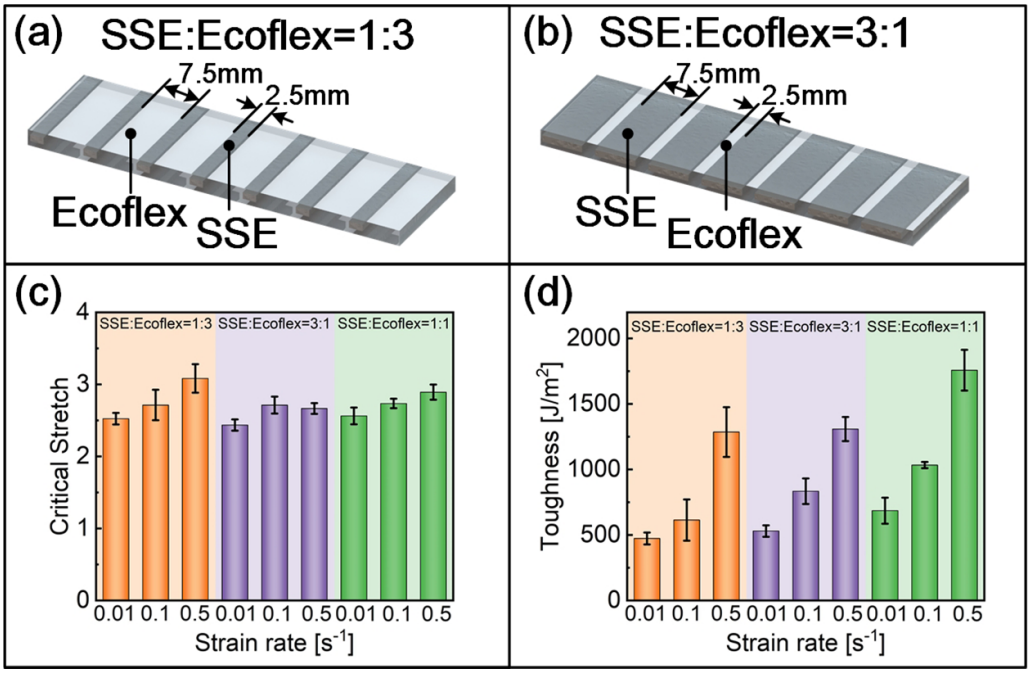

Figure A4. The fracture mechanical behavior of samples with different Ecoflex and SSE contents. (a), (b) The schematic of specimen geometry for low content of SSE (SSE: Ecoflex = 1:3) and high content of SSE (SSE: Ecoflex = 3:1). (c), (d) The calculated critical stretch and fracture toughness for SSE: Ecoflex = 1:3, SSE: Ecoflex = 3:1, and SSE: Ecoflex = 1:1 at the strain rate of 0.01 s^{-1}, 0.1 s^{-1}, and 0.5 s^{-1} (Error bars: S.D., $n = 3$).

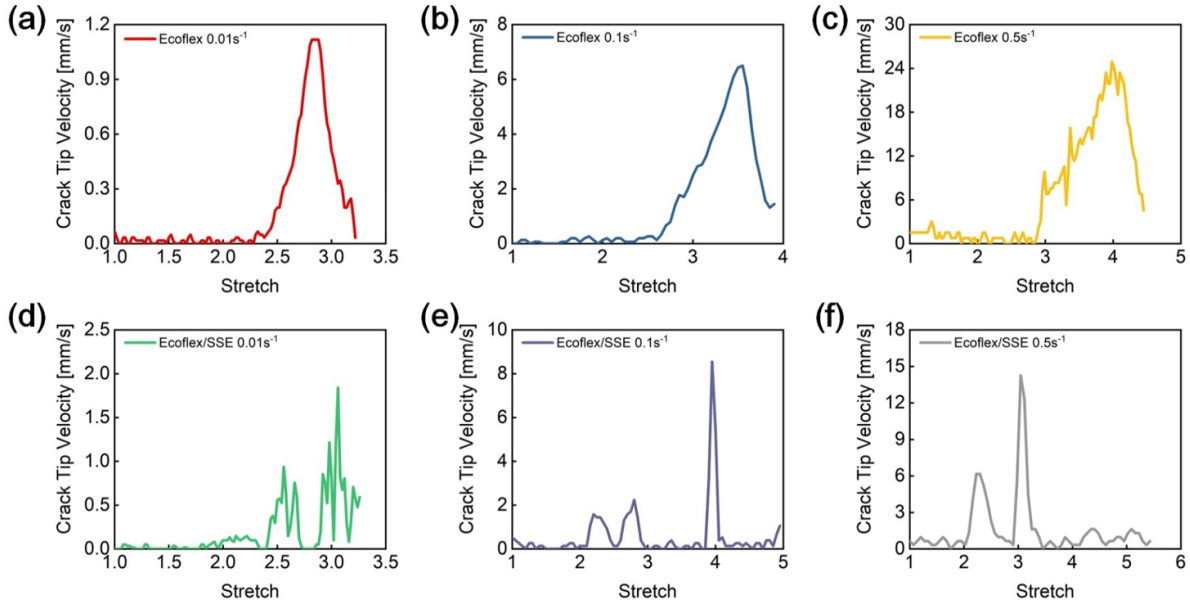

Figure A5. The curves of crack tip velocity vs. stretch during the crack propagation for the homogeneous Ecoflex: (a)–(c) Homogeneous Ecoflex at the strain rates of 0.01 s^{-1}, 0.1 s^{-1}, and 0.5 s^{-1}. (d)–(f) Ecoflex/SSE composite at the strain rate of 0.01 s^{-1}, 0.1 s^{-1}, and 0.5 s^{-1}.

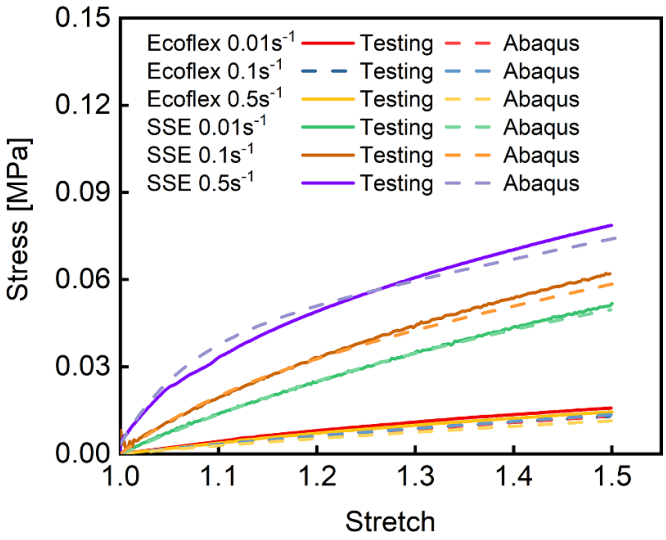

Figure A6. The comparison of the uniaxial tensile FEA simulation results of Ecoflex and SSE elastomers with the experimental results at the testing stretch range.

Table A1. The material parameters of Ecoflex and SSE in Abaqus.

Specimen	Strain rate (s^{-1})	μ (MPa)		b (MPa)	
Ecoflex	0.01	0.01175		0.15903	
	0.1	0.01219		0.18454	
	0.5	0.01044		0.13483	
Specimen	Strain rate (s^{-1})	E_1 (MPa)	E_2 (MPa)	H (MPa s)	Poisson's ratio
SSE	0.01	0.12904	0.14957	15.33948	0.48000
	0.1	0.21170	0.26345	0.45318	0.48000
	0.5	0.15119	0.60043	0.08735	0.48000

ORCID iDs

Shouhu Xuan https://orcid.org/0000-0002-8232-9736
Xinglong Gong https://orcid.org/0000-0001-6997-9526

References

[1] Yao S S, Ren P, Song R Q, Liu Y X, Huang Q J, Dong J Y, O'Connor B T and Zhu Y 2020 Nanomaterial-enabled flexible and stretchable sensing systems: processing, integration, and applications *Adv. Mater.* **32** 1902343
[2] Li Y J, Zhang K L, Geng Q, Nie M, Wang Q, Huang Z X, Wu Z H and Pi L 2021 Helically intersected conductive network design for wearable electronic devices: from theory to application *ACS Appl. Mater. Interfaces* **13** 11480–8
[3] Yuan F, Liu S, Zhou J Y, Wang S, Wang Y, Xuan S H and Gong X L 2021 Smart touchless triboelectric nanogenerator towards safeguard and 3D morphological awareness *Nano Energy* **86** 106071
[4] Wang J X, Gao D and Lee P S 2021 Recent progress in artificial muscles for interactive soft robotics *Adv. Mater.* **33** 2003088
[5] Gupta U, Qin L, Wang Y Z, Godaba H and Zhu J 2019 Soft robots based on dielectric elastomer actuators: a review *Smart Mater. Struct.* **28** 103002
[6] Baumgartner M *et al* 2020 Resilient yet entirely degradable gelatin-based biogels for soft robots and electronics *Nat. Mater.* **19** 1102–9
[7] Zhu M *et al* 2022 A mechanically interlocking strategy based on conductive microbridges for stretchable electronics *Adv. Mater.* **34** 2101339
[8] Yuan F, Liu S, Zhou J Y, Fan X W, Wang S and Gong X L 2020 A smart Kevlar-based triboelectric nanogenerator with enhanced anti-impact and self-powered sensing properties *Smart Mater. Struct.* **29** 125007
[9] Yi Y, Chiao M and Wang B 2021 An electrochemically actuated drug delivery device with *in-situ* dosage sensing *Smart Mater. Struct.* **30** 055003
[10] Arun Y, Ghosh R and Domb A J 2021 Biodegradable hydrophobic injectable polymers for drug delivery and regenerative medicine *Adv. Funct. Mater.* **31** 2010284
[11] Nonoyama T, Lee Y W, Ota K, Fujioka K, Hong W and Gong J P 2020 Instant thermal switching from soft hydrogel to rigid plastics inspired by thermophile proteins *Adv. Mater.* **32** 1905878
[12] Yu C T, Guo H L, Cui K P, Li X Y, Ye Y N, Kurokawa T and Gong J P 2020 Hydrogels as dynamic memory with forgetting ability *Proc. Natl Acad. Sci. USA* **117** 18962–8
[13] Liu X Y, Yang Y Y, Inda M E, Lin S T, Wu J J, Kim Y H, Chen X Y, Ma D C, Lu T K and Zhao X H 2021 Magnetic living hydrogels for intestinal localization, retention, and diagnosis *Adv. Funct. Mater.* **31** 2010918
[14] Wu S J, Yuk H W, Wu J J, Nabzdyk C S and Zhao X H 2021 A multifunctional origami patch for minimally invasive tissue sealing *Adv. Mater.* **33** 2007667
[15] Liu X, Wu J P, Qiao K K, Liu G H, Wang Z J, Lu T Q, Suo Z G and Hu J 2022 Topoarchitected polymer networks expand the space of material properties *Nat. Commun.* **13** 1622

[16] Yang J W, Steck J, Bai R B and Suo Z G 2020 Topological adhesion II. Stretchable adhesion *Extreme Mech. Lett.* **40** 100891

[17] Kim J S, Zhang G G, Shi M X and Suo Z G 2021 Fracture, fatigue, and friction of polymers in which entanglements greatly outnumber cross-links *Science* **374** 212–6

[18] Hu Y J *et al* 2021 Graphene oxide encapsulating liquid metal to toughen hydrogel *Adv. Funct. Mater.* **31** 2106761

[19] Zhang J Q, Huang C, Zhu Y, Huang G S and Wu J R 2021 Toughening polyisoprene rubber with sacrificial bonds: the interplay between molecular mobility, energy dissipation and strain-induced crystallization *Polymer* **231** 124114

[20] King D R, Takahashi R, Ikai T, Fukao K, Kurokawa T and Gong J P 2020 Anisotropic double-network hydrogels via controlled orientation of a physical sacrificial network *ACS Appl. Polym. Mater.* **2** 2350–8

[21] Liu J, Lin S T, Liu X Y, Qin Z Y, Yang Y Y, Zang J F and Zhao X H 2020 Fatigue-resistant adhesion of hydrogels *Nat. Commun.* **11** 1071

[22] Wang P R, Berry D B, Song Z Q, Kiratitanaporn W, Schimelman J, Moran A, He F, Xi B, Cai S Q and Chen S C 2020 3D printing of a biocompatible double network elastomer with digital control of mechanical properties *Adv. Funct. Mater.* **30** 1910391

[23] Song C, Chen B H, Hwang J, Lee S, Suo Z G and Ahn H 2021 A printed highly stretchable supercapacitor by a combination of carbon ink and polymer network *Extreme Mech. Lett.* **49** 101459

[24] Li C H, Yang H, Suo Z G and Tang J D 2020 Fatigue-resistant elastomers *J. Mech. Phys. Solids* **134** 103751

[25] Xiang C P, Wang Z J, Yang C H, Yao X, Wang Y C and Suo Z G 2020 Stretchable and fatigue-resistant materials *Mater. Today* **34** 7–16

[26] Zhao C Y, Gong X L, Wang S, Jiang W Q and Xuan S H 2020 Shear stiffening gels for intelligent anti-impact applications *Cell Rep. Phys. Sci.* **1** 100266

[27] Jacob G C, Starbuck J M, Fellers J F, Simunovic S and Boeman R G 2005 The effect of loading rate on the fracture toughness of fiber reinforced polymer composites *J. Appl. Polym. Sci.* **96** 899–904

[28] Boland C S *et al* 2016 Sensitive electromechanical sensors using viscoelastic graphene-polymer nanocomposites *Science* **354** 1257–60

[29] Zhao C Y, Wang Y, Ni M Y, He X K, Xuan S H and Gong X L 2021 Dynamic behavior of impact hardening elastomer: a flexible projectile material with unique rate-dependent performance *Composites* A **143** 106285

[30] Tang M, Zheng P, Wang K Q, Qin Y J, Jiang Y Z, Cheng Y R, Li Z and Wu L M 2019 Autonomous self-healing, self-adhesive, highly conductive composites based on a silver-filled polyborosiloxane/polydimethylsiloxane double-network elastomer *J. Mater. Chem.* A **7** 27278–88

[31] Zhou J Y, Wang S, Yuan F, Zhang J S, Liu S, Zhao C Y, Wang Y and Gong X L 2021 Functional Kevlar-based triboelectric nanogenerator with impact energy-harvesting property for power source and personal safeguard *ACS Appl. Mater. Interfaces* **13** 6575–84

[32] Agnelli S, Balasooriya W, Bignotti F and Schrittesser B 2020 On the experimental measurement of fracture toughness in SENT rubber specimens *Polym. Test.* **87** 106508

[33] Blaber J, Adair B and Antoniou A 2015 Ncorr: open-source 2D digital image correlation matlab software *Exp. Mech.* **55** 1105–22

[34] Wang Z J, Xiang C P, Yao X, Le Floch P, Mendez J and Suo Z G 2019 Stretchable materials of high toughness and low hysteresis *Proc. Natl Acad. Sci. USA* **116** 5967–72

[35] Janbaz S, Narooei K, Van Manen T and Zadpoor A A 2020 Strain rate-dependent mechanical metamaterials *Sci. Adv.* **6** eaba0616

[36] Corre T, Coret M, Verron E, Leble B and Le Lay F 2020 Experimental full field analysis for dynamic fracture of elastomer membranes *Int. J. Fract.* **224** 83–100

[37] Kolvin I, Kolinski J M, Gong J P and Fineberg J 2018 How supertough gels break *Phys. Rev. Lett.* **121** 135501

[38] Morishita Y, Tsunoda K and Urayama K 2017 Crack-tip shape in the crack-growth rate transition of filled elastomers *Polymer* **108** 230–41

[39] Goldman T, Livne A and Fineberg J 2010 Acquisition of inertia by a moving crack *Phys. Rev. Lett.* **104** 114301

[40] Kazem N, Bartlett M D and Majidi C 2018 Extreme toughening of soft materials with liquid metal *Adv. Mater.* **30** 1706594

[41] Bartlett M D, Kazem N, Powell-Palm M J, Huang X N, Sun W H, Malen J A and Majidi C 2017 High thermal conductivity in soft elastomers with elongated liquid metal inclusions *Proc. Natl Acad. Sci. USA* **114** 2143–8

[42] Knowles J K 1977 Finite anti-plane shear field near tip of a crackfor a class of incompressible elastic solids *Int. J. Fract.* **13** 611–39

[43] Qi Y, Zou Z A, Xiao J L and Long R 2019 Mapping the nonlinear crack tip deformation field in soft elastomer with a particle tracking method *J. Mech. Phys. Solids* **125** 326–46

[44] Cross R 2012 Elastic and viscous properties of silly putty *Am. J. Phys.* **80** 870–5

[45] Fleck N A, Kang K J and Ashby M F 1994 Overview no. 112—the cyclic properties of engineering materials *Acta Metall. Mater.* **42** 365–81

[46] Lin S T, Liu J, Liu X Y and Zhao X H 2019 Muscle-like fatigue-resistant hydrogels by mechanical training *Proc. Natl Acad. Sci. USA* **116** 10244–9

[47] Lin S T *et al* 2019 Anti-fatigue-fracture hydrogels *Sci. Adv.* **5** eaau8528

[48] Genesky G D and Cohen C 2010 Toughness and fracture energy of PDMS bimodal and trimodal networks with widely separated precursor molar masses *Polymer* **51** 4152–9

[49] Marco-Dufort B, Iten R and Tibbitt M W 2020 Linking molecular behavior to macroscopic properties in ideal dynamic covalent networks *J. Am. Chem. Soc.* **142** 15371–85

[50] Wang Y P, Ding L, Zhao C Y, Wang S, Xuan S H, Jiang H and Gong X L 2018 A novel magnetorheological shear-stiffening elastomer with self-healing ability *Compos. Sci. Technol.* **168** 303–11